Inorganic Chemistry

Article

pubs.acs.org/IC

Structural, Optical, and Electrical Characterization of Yttrium-Substituted $BiFeO_3$ Ceramics Prepared by Mechanical Activation

Antonio Perejón,*[,†,‡] Eva Gil-González,[†] Pedro E. Sánchez-Jiménez,[†] José M. Criado,[†] and Luis A. Pérez-Maqueda*[,†]

[†]Instituto de Ciencia de Materiales de Sevilla, Consejo Superior de Investigaciones Científicas−Universidad de Sevilla. Calle Américo Vespucio 49, Sevilla 41092, Spain

[‡]Departamento de Química Inorgánica, Facultad de Química, Universidad de Sevilla, Sevilla 41071, Spain

Supporting Information

ABSTRACT: Ceramics of $Bi_{1-x}Y_xFeO_3$ solid solutions (x = 0.02, 0.07, and 0.10) have been prepared by mechanical activation followed by sintering. The effect of yttrium content on the structural, electrical, and optical properties of the materials has been studied. Thus, single-phase solid solutions with rhombohedral *R*3*c* structure have been achieved for x = 0.02 and 0.07, while for x = 0.10 the main *R*3*c* phase has been detected together with a small amount of the orthorhombic *Pbnm* phase. Multiferroic properties of the samples, studied by differential scanning calorimetry (DSC), showed that both T_N and T_C (temperatures of the antiferromagnetic−paramagnetic and ferroelectric−paraelectric transitions, respectively) decrease with increasing yttrium content. The nature of the ferroelectric−paraelectric transition has been studied by temperature-dependent X-ray diffraction (XRD), which revealed rhombohedral *R*3*c* to orthorhombic *Pbnm* phase transitions for x = 0.07 and 0.10. On the other hand, for x = 0.02 the high-temperature phase was indexed as *Pnma*. Optical properties of the samples, as studied by diffuse reflectance spectroscopy, showed low optical band gap that decreases with increasing yttrium content. Prepared ceramics were highly insulating at room temperature and electrically homogeneous, as assayed by impedance spectroscopy, and the conductivity increased with x.

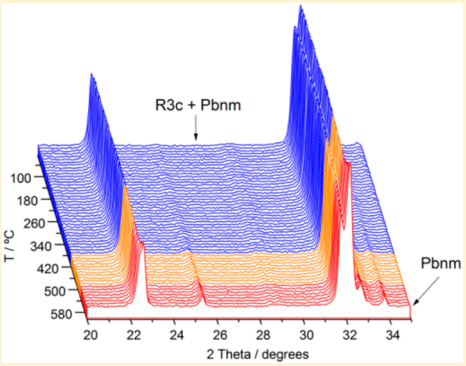

1. INTRODUCTION

Multiferroic materials are characterized by the presence, at the same time, of two of the following properties: ferroelectricity, ferromagnetism, and ferroelasticity. These materials are interesting due to their applications as magnetoelectric sensors, transducers, or multiple-state memory elements.[1−7] $BiFeO_3$ is probably the best-studied multiferroic material because it is ferroelectric and antiferromagnetic above room temperature, with T_N and T_C at about 370 and 830 °C, respectively,[8,9] and it is well-known that it presents a rhombohedrally distorted perovskite structure at room temperature with space group *R*3*c*. However, the preparation of $BiFeO_3$ in bulk for future applications presents several problems related to the presence of defects and nonstoichiometry and therefore the formation of undesired impurity phases, mainly $Bi_{25}FeO_{39}$ and $Bi_2Fe_4O_9$. Thus, $BiFeO_3$ obtained by different methods usually presents leakage current and dielectric loss problems together with a small spontaneous polarization value.[10,11]

To overcome these problems, recent works have focused on preparation of this compound by different methods.[12−15] Another way to improve the properties of $BiFeO_3$ is preparation of mixtures of $BiFeO_3$ with other oxides,[16−22] and the addition of substituents in the positions of both Bi and Fe.[23,24] These compounds have been widely studied, with special emphasis on bismuth substitution by rare earth elements, transition metals, and alkaline earth metals, because it has been reported that this avoids the formation of the undesired phases during the synthesis and improves the magnetic and dielectric properties of the material.[25−30] Thus, substitution of Bi^{3+} ions by these elements breaks the long-range, spin cycloid superstructure of the antiferromagnetic sublattice responsible for cancellation of magnetization of the perovskite.[31]

Yttrium-substituted $BiFeO_3$ has attracted interest in the past few years due to the magnetic, optical, and catalytic properties of these compounds. However, the presence of different phases has been observed for the system $Bi_{1-x}Y_xFeO_3$ as the yttrium content (x) increases, with disagreement over the value of x that induces phase transitions and the structures that the systems adopt. Thus, while it has been proved that for $x < 0.1$ the system presents a rhombohedral *R*3*c* structure, it has been suggested that for $x \sim 0.1$ a structural phase transition takes place, because the diffraction patterns tend to that of orthorhombic $LaFeO_3$ (*Pnma*).[32−34] Other authors propose that for x = 0.1 the *R*3*c* phase is maintained,[35,36] and a tetragonal phase is obtained for x = 0.15.[35] However, it has also been proposed, for materials prepared by different methods,

Received: July 23, 2015
Published: October 2, 2015

DOI: 10.1021/acs.inorgchem.5b01654
Inorg. Chem. 2015, 54, 9876−9884

that the samples present the $R3c$ phase up to $x = 0.2$,[37−40] and the appearance of other phases occurs for higher yttrium content.[41]

Different methods have been employed for the synthesis of the $Bi_{1-x}Y_xFeO_3$ system: conventional and modified solid-state reactions,[37−39] citrate-gel method and modified Pechini method,[32−34,36] tartaric acid modified sol−gel method,[41] metal ion ligand complex-based precursor−solution evaporation method[35] and coprecipitation methods.[40] In general, the samples obtained are not phase-pure, because it is difficult to avoid the formation of impurity phases, mainly $Bi_2Fe_4O_9$.

Despite the presence of secondary phases, the dielectric, magnetic, and photocatalytic properties of the samples have been studied and an enhancement in these properties, with respect to $BiFeO_3$, is generally reported. Electrical transport properties of yttrium-substituted $BiFeO_3$ samples obtained by a modified Pechini method were studied by Mukherjee et al.[36] They found, by direct and alternating current (dc and ac) measurements, that the resistivity and dielectric permittivity increase with increasing yttrium content and that the dielectric permittivity of the samples depends on grain and grain boundary resistance. Impedance measurements have also been made by Minh and Thang,[37] who showed that the samples present microstructural inhomogeneity as grain and grain boundary effects were observed and that yttrium substitution improved the boundary impedance.

Mechanical activation produces nanostructured materials by using mechanical energy to activate chemical reactions and particle reduction.[42−45] The objective of this work is the preparation of single-phase samples of the system $Bi_{1-x}Y_xFeO_3$ by mechanical activation followed by sintering and the characterization of the products by XRD, Raman spectroscopy, SEM, DSC, dilatometry, and impedance spectroscopy.

2. EXPERIMENTAL SECTION

2.1. Sample Preparation. Samples were synthesized from the commercially available oxides Bi_2O_3 (Sigma−Aldrich 223891-500G, 10 μm, 99.9% purity), Fe_2O_3 (Sigma−Aldrich 310050-500G, <5 μm, ≥99% purity), and Y_2O_3 (Strem Chemicals 93-3911. 99.9% purity). It was determined by thermogravimetry (TG) that the starting oxides did not require drying.

Samples of the system $Bi_{1-x}Y_xFeO_3$ were prepared by mechanical activation followed by sintering. The pristine oxides were mechanically ground for 6 h in 7 bar of O_2 in a modified planetary mill, Pulverisette 7 (Fritsch, Idar-Oberstein, Germany). It has been recently demonstrated that oxygen acts as an inhibitor of bismuth reduction by the iron of the grinding medium.[46] Thus, a rotary valve incorporated into the mill connected the jar to the gas cylinder during milling, maintaining the pressure constant inside the jar even if the gas was consumed. Jars were purged with oxygen several times and then filled to the desired pressure. Hardened steel jar, 80 cm^3 in volume, and nine balls, 15 mm in diameter, were used in the experiments, and the powder-to-ball mass ratio was set at 1:20, which required approximately 6 g of starting oxides. The spinning rate of the supporting disc was set at 700 rpm. A kinematic study of the balls and jars during the mechanical treatment gave the following values for corrected impact energy and total power: $\Delta E^* = 82$ mJ/hit and $P = 25.8$ W. Then 400 mg of the resulting materials for each composition were pressed into pellets in a hardened steel die, 6.35 mm diameter, and a uniaxial pressing of 0.93 GPa was applied. The green pellets were subjected to sintering at 850 °C for 1 min.

2.2. Characterization. X-ray diffraction (XRD) patterns were collected with a Panalytical X'Pert Pro diffractometer working at 45 kV and 40 mA, using Cu Kα radiation and equipped with an X'Celerator detector and a graphite-diffracted beam monochromator. Celref software was used to determine the lattice parameters of the compounds. FullProf software was used for Rietveld refinement.[47,48] The background was refined by use of a six-order polynomial function and a pseudo-Voigt function with axial divergence asymmetry profile was employed to refine peak shapes.

Raman spectra of the samples were collected with a dispersive Horiba Jobin Yvon LabRam HR800 microscope with a 20 mW green laser (532.14 nm) and a 100× objective with a confocal pinhole of 10 μm.

Sintering was followed by dilatometric analysis, placing the green pellets in a Linseis TMA model PT1000 and heating in 100 $cm^3 \cdot min^{-1}$ airflow with a 10 °C·min^{-1} heating rate from 250 to 850 °C. Density of the ceramics was determined by the Archimedes method, with water as the immersion liquid. Microstructure of the resulting ceramics was studied by scanning electron microscopy (SEM) on a Hitachi S-4800 microscope equipped with an energy-dispersive X-ray spectrometer (EDX) attachment. Pellets were polished and thermally etched for 30 min at 90% of the sintering temperature to reveal the grain boundaries.

Differential scanning calorimetry (DSC) curves were recorded in air (100 $cm^3 \cdot min^{-1}$) on a DSC instrument and a simultaneous TG/DSC instrument (Q200 and Q600 SDT, respectively; TA Instruments, Crawley, U.K.). The experiments were performed at a heating/cooling rate of 10 °C·min^{-1}, from 0 to 850 °C in open alumina pans. The temperatures of the transitions were taken as the onset of the peaks.

Temperature-dependent X-ray diffraction patterns were recorded in 100 $cm^3 \cdot min^{-1}$ airflow in a Philips X'Pert Pro diffractometer equipped with a high-temperature Anton-Paar camera working at 45 kV and 40 mA, using Cu Kα radiation and equipped with an X'Celerator detector and a graphite-diffracted beam monochromator.

For electrical measurements, the two parallel surfaces of the sintered discs were covered with gold by means of a sputtering device to improve electrical contact with the platinum electrodes. Impedance measurements used a phase-sensitive multimeter (PSM1735, Newton4th Ltd.) over the frequency range 5 Hz−5 MHz, with an ac measuring voltage of 100 mV and from room temperature to 380 °C. The data were corrected for pellet geometry.

UV−visible spectra were recorded in the scan range 250−800 nm on a Shimadzu spectrophotometer (model AV2101), in the diffuse reflectance mode (R), which was transformed to a magnitude proportional to the extinction coefficient (K) by means of the Kubelka−Munk function. Samples were mixed with $BaSO_4$, which was used as a white standard since it does not absorb in the UV−vis radiation range.

3. RESULTS AND DISCUSSION

Figure 1 shows the as-obtained XRD patterns of the products of mechanical activation. Peaks are broad because the crystallite size is nanometric after a mechanical activation of 6 h.[46,49] The XRD pattern for composition $x = 0.10$ presents a very weak peak at about 25.5° (Figure 1c), which could be related to either a phase transition in the material or the presence of a secondary phase.

Figure 2 presents the dilatometric curve corresponding to sintering of the green pellet of composition $x = 0.02$. Thermal expansion is observed in the curve from room temperature to 425 °C, and then the pellet begins to contract in a number of overlapping steps, with a large contraction from 800 °C. Dilatometric curves for green pellets of compositions $x = 0.07$ and 0.10 present similar behavior to the pellet with $x = 0.02$, with the initial thermal expansion and contraction from about 425 °C (see Supporting Information, Figures S1 and S2). This behavior also has been observed for La-substituted samples.[49] The relative densities of the sintered pellets, calculated by Archimedes' method, were 92.1%, 85.4%, and 84.3% for $x = 0.02$, 0.07, and 0.10, respectively. Therefore, a decrease in density is obtained as yttrium content increases.

Figure 3 shows the XRD patterns of the sintered samples for every composition, in the range 20−50° 2θ. Samples $x = 0.02$

DOI: 10.1021/acs.inorgchem.5b01654
Inorg. Chem. 2015, 54, 9876−9884

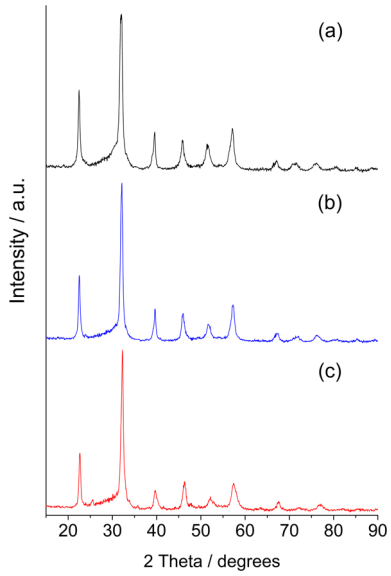

Figure 1. XRD patterns of powders obtained after mechanical activation of stoichiometric amounts of pristine oxides in oxygen (7 bar) for different compositions: (a) $Bi_{0.98}Y_{0.02}FeO_3$, (b) $Bi_{0.93}Y_{0.07}FeO_3$, and (c) $Bi_{0.90}Y_{0.10}FeO_3$.

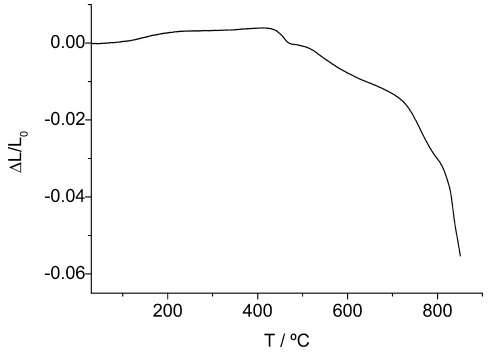

Figure 2. Dilatometric curve for $Bi_{0.98}Y_{0.02}FeO_3$ pellet.

and 0.07 present similar patterns, and also similar to that of $BiFeO_3$,[46] which means that, essentially, single-phase materials have been prepared in both cases, with no evidence of any other impurity phases.

Sample $x = 0.10$ presents a weak peak at 25.5°, as was already observed for the ground material (Figure 1c), and the presence of other small features confirms either a partial structural phase transition or the existence of a secondary phase.

The patterns were analyzed by the Rietveld method in order to obtain qualitative and semiquantitative crystallographic information on the phases. Compositions $x = 0.02$ and 0.07 could be refined well by considering rhombohedral structure with space group *R*3*c*, as shown in Table 1 (see also Figures S3 and S4 in Supporting Information). These results are consistent with those reported by other authors for samples prepared by other methods.[32,33,50] The indexing of composition $x = 0.10$ was tested in the space groups *R*3*c*, *Pnma*, *Pn*21*a*, and *Imma*, and none of these accounted for all the observed peaks, which causes high reliability factor values. For this reason, combinations of different space groups were tested, and the best refinement was obtained for *R*3*c* + *Pbnm* space groups. This structural model accounts for all the features observed in the XRD pattern (Figure 4 and Table 1). Thus, from the

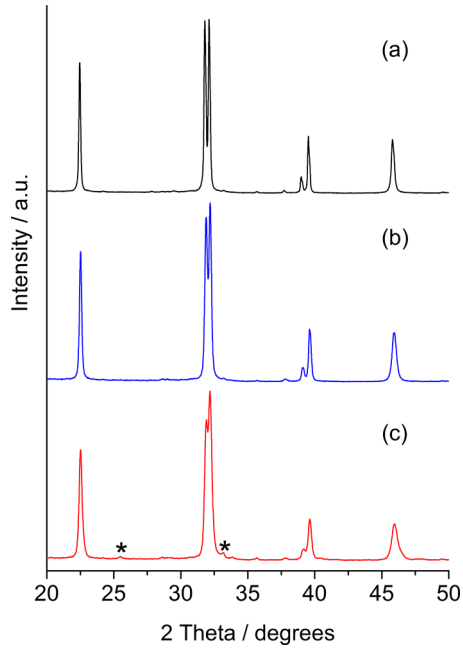

Figure 3. XRD patterns of samples obtained after sintering mechanically activated powders: (a) $Bi_{0.98}Y_{0.02}FeO_3$, (b) $Bi_{0.93}Y_{0.07}FeO_3$, and (c) $Bi_{0.90}Y_{0.10}FeO_3$.

Rietveld analysis, the weight percent of *Pbnm* phase was estimated to be around just 6%, and therefore $x \sim 0.094$. The coexistence of *R*3*c* with other space groups for $Bi_{1-x}Ln_xFeO_3$ samples has been reported by several authors for different substituents and compositions.[51−55] It is important to take into account that *Pbnm* is a nonstandard setting. The space groups *Pnma* and *Pbnm* are structurally equivalent and differ only in the choice of the unique axis. Thus, *Pbnm* can be described by an out-of-phase tilting of the FeO_6 octahedra in the *a* and *b* planes and an in-phase tilt of the FeO_6 octahedra in the *c* direction.[56]

The microstructure of the prepared pellets was studied by SEM (Figure 5). Pellets were thermally etched for 30 min at 90% of the sintering temperature to reveal the grain boundaries. In general, the grains present different sizes and are irregular. Moreover, the average grain size decreases with increasing yttrium content, from 1.2 ± 0.5 μm for $x = 0.02$ and approximately 0.8 ± 0.4 μm for $x = 0.07$ to 0.5 ± 0.4 μm for $x = 0.10$. A similar decrease in grain size with increasing substituent content has been observed for sintered La-substituted samples.[57] The table portion of Figure 5 shows the elemental composition of the samples, determined by semiquantitative analysis of EDX spectra of each composition. When one takes into account that the nominal atomic composition Fe/Y/Bi is 50.0/1.0/49.0 for $x = 0.02$, 50.0/3.5/46.5 for $x = 0.07$, and 50.0/5.0/45 for $x = 0.10$, it is clear that the materials have maintained in all cases the nominal stoichiometry after the mechanical activation and sintering processes.

Figure 6 presents Raman spectra at room temperature for the three compositions. The selection rules for Raman-active modes in a rhombohedral *R*3*c* symmetry give rise to 13 active modes: four A1 modes and nine E modes. The spectrum for $x = 0.02$ shows 10 lines, four of which can be attributed to A1 modes (at 160, 174, 226, and 412 cm^{-1}) and six of which correspond to E modes (at 261, 292, 370, 479, 529, and 619

DOI: 10.1021/acs.inorgchem.5b01654
Inorg. Chem. 2015, 54, 9876−9884

Table 1. Rietveld Refinement Structural Parameters[a]

	$Bi_{0.98}Y_{0.02}FeO_3$	$Bi_{0.93}Y_{0.07}FeO_3$	$Bi_{0.90}Y_{0.10}FeO_3$	
space group	*R3c*	*R3c*	*R3c*	*Pbnm*
a (Å)	5.57702(1)	5.56776(5)	5.56321(3)	5.42433(4)
b (Å)	5.57702(1)	5.56776(5)	5.56321(3)	5.62842(7)
c (Å)	13.86314(2)	13.83335(5)	13.81320(1)	7.84045(8)
		Atomic Positions		
Bi/Y	0.00, 0.00, 0.00	0.00, 0.00, 0.00	0.00, 0.00, 0.00	0.0020(6), 0.0510(9), 0.25
Fe	0.00, 0.00, 0.2212(3)	0.00, 0.00, 0.2229(4)	0.00, 0.00, 0.2232(3)	0.00, 0.50, 0.50
O(1)	0.4420(1), 0.0065(5), 0.9522(2)	0.4437(1), 0.0129(4), 0.9523(1)	0.4656(4), 0.0308(5), 0.9476(6)	0.0854(3), 0.4899(5), 0.25
O(2)				0.6754(6), 0.2951(8), 0.0110(1)
		Bond Angle (deg)		
Fe−O(1)−Fe	156.4	154.8	152.3	142.9
Fe−O(2)−Fe				147.1
		Confidence Factors		
χ^2	3.28	2.59	2.80	
Rwp	15.5	14.2	14.0	

[a]Determined from XRD patterns of powders of the system $Bi_{(1-x)}Y_xFeO_3$, obtained after 6 h of mechanical activation and subsequent sintering at 850 °C.

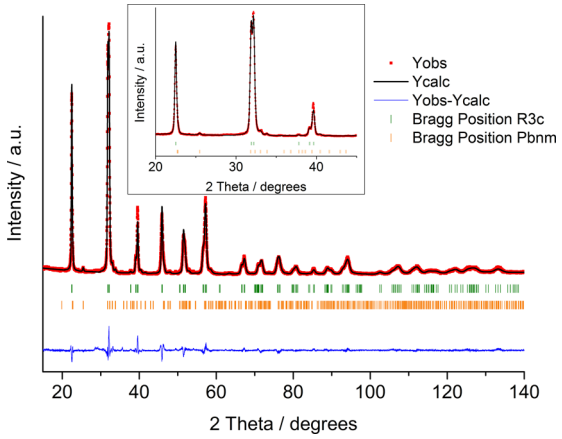

Figure 4. XRD pattern of $Bi_{0.90}Y_{0.10}FeO_3$ obtained after 6 h of mechanical activation and subsequent sintering at 850 °C (dots). Solid lines are the fit from the Rietveld refinement. (Inset) Expanded section in the range 20−45° 2θ.

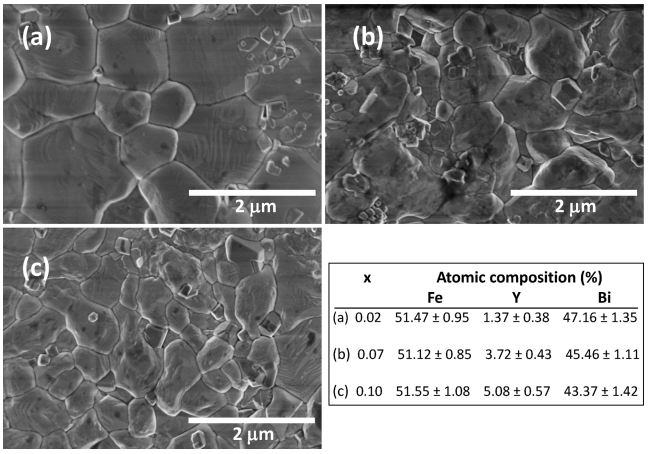

x	Atomic composition (%) Fe	Y	Bi
(a) 0.02	51.47 ± 0.95	1.37 ± 0.38	47.16 ± 1.35
(b) 0.07	51.12 ± 0.85	3.72 ± 0.43	45.46 ± 1.11
(c) 0.10	51.55 ± 1.08	5.08 ± 0.57	43.37 ± 1.42

Figure 5. SEM micrographs of pellets obtained after 6 h of mechanical activation and subsequent calcination at 850 °C.

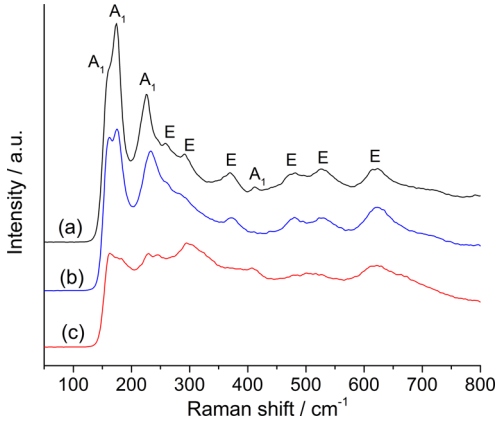

Figure 6. Raman spectra of samples obtained after 6 h of mechanical activation and subsequent calcination at 850 °C: (a) $Bi_{0.98}Y_{0.02}FeO_3$, (b) $Bi_{0.93}Y_{0.07}FeO_3$, and (c) $Bi_{0.90}Y_{0.10}FeO_3$.

cm^{-1}). The low Raman shift bands are associated with the relative movement of Bi cations against the FeO_6 octahedron, while high Raman shift bands (above 200 cm^{-1}) correspond to internal vibrations of the FeO_6 octahedron. The spectrum for x = 0.02 is characteristic of *R3c* symmetry with small deviations, probably due to the distortions caused in the structure by yttrium substitution. The tolerance factor is defined as[58]

$$t = \frac{(r_A + r_O)}{\sqrt{2}(r_B + r_O)} \quad (1)$$

where r_A is the average of ionic radii of Bi^{3+} and Y^{3+}, r_O is the ionic radius of O^{2-}, and r_B is the ionic radius of Fe^{3+}. Thus, the value of the tolerance factor is reduced with increasing yttrium content (with an ionic radius of 1.019 according to Shannon[59]) from 0.888 for x = 0.02 to 0.883 for x = 0.10, which indicates that yttrium substitution causes distortions in the $BiFeO_3$ structure. These distortions modify the Raman spectra, as observed by other authors for different substituents.[37,41,49,60,61] Compositions x = 0.07 and 0.10 present Raman spectra similar to that of x = 0.02, but the low Raman shift bands decrease in intensity due to the reduced number of Bi−O bonds as the yttrium content increases, which demonstrates that yttrium atoms are effectively occupying the A sites in the perovskite. Moreover, for x = 0.10, the band at 370 cm^{-1} almost disappears and the bands at 479 and 529 cm^{-1} appear overlapped.

DOI: 10.1021/acs.inorgchem.5b01654
Inorg. Chem. 2015, 54, 9876−9884

Multiferroic character and phase transitions of the samples were studied by a combination of DSC, dilatometry, and temperature-dependent XRD. Figure 7 shows DSC traces

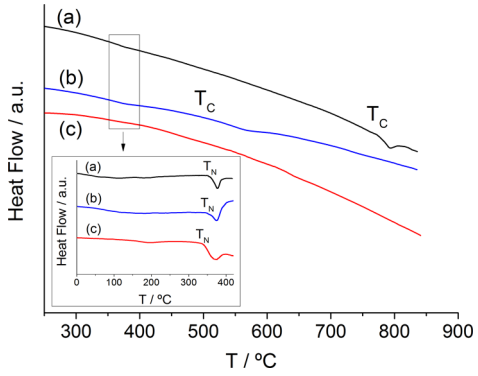

Figure 7. DSC traces of samples obtained after 6 h of mechanical activation and subsequent sintering at 850 °C: (a) $Bi_{0.98}Y_{0.02}FeO_3$, (b) $Bi_{0.93}Y_{0.07}FeO_3$, and (c) $Bi_{0.90}Y_{0.10}FeO_3$. (Inset) Temperature range from 0 to 420 °C, where the antiferromagnetic−paramagnetic transition takes place.

obtained upon heating of small pieces of pellets, where the first peak corresponds to the antiferromagnetic−paramagnetic transition (T_N) and the second to the ferroelectric−paraelectric transition (T_C). The inset presents the DSC traces in the temperature range from 0 to 420 °C, where the only peak observed for each composition corresponds to T_N, which is a weak effect with onsets at 363 and 354 °C for x = 0.02 and 0.07, respectively, while for x = 0.10 the peak is broader with the onset at ∼349.5 °C. Thus, a small decrease in T_N is observed as the yttrium content increases. The ferroelectric−paraelectric transition also decreases with increasing yttrium content, as observed by other authors for yttrium-substituted $BiFeO_3$,[34,36] from 775 °C for x = 0.02 to 530 °C for x = 0.07 (Table 2). This transition appears as a broad band for x = 0.07. However, the ferroelectric−paraelectric transition is not observed by DSC for x = 0.10.

Dilatometric curves were registered upon heating from 250 to 850 °C for the dense sintered pellets (Figure 8a). Curves show a considerable volume reduction at T_C for x = 0.02 and 0.07 and at identical temperatures as observed by DSC, but composition x = 0.10 presents a more gradual decrease in volume, from 420 to about 525 °C, suggesting that the phase transition is slow and takes place over a wide range of temperatures (Table 2). Figure 8b presents the composition dependence of T_C and T_N for x = 0.02 and 0.07. From the Néel temperature determined by DSC and the Curie temperature obtained by dilatometry, the amount of *R*3*c* phase for composition x = 0.10 was estimated to be 93% if linear dependences of T_N and T_C on x are considered. This value is in

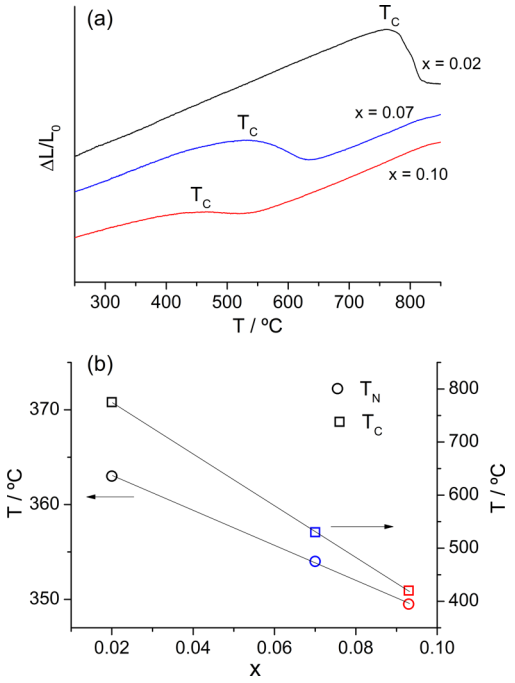

Figure 8. (a) Dilatometric curves of dense pellets prepared by mechanical activation and subsequent sintering at 850 °C. (b) Composition dependence of T_N and T_C for the three prepared ceramics.

good agreement with the value of x calculated by Rietveld refinement (Figure 4).

These results are confirmed by temperature-dependent XRD. Figure 9 presents XRD patterns of $Bi_{0.90}Y_{0.10}FeO_3$ recorded in

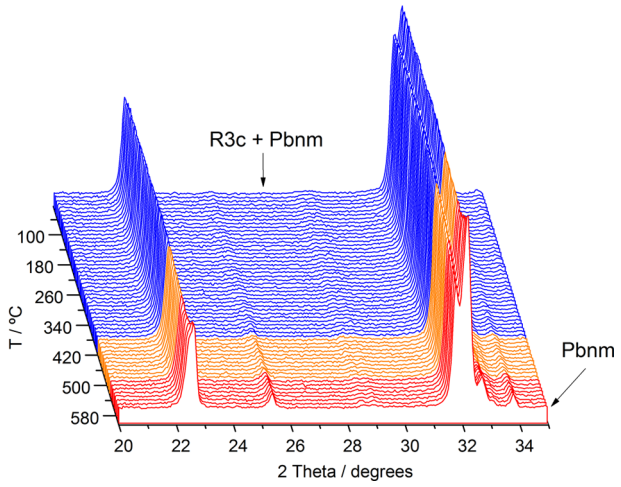

Figure 9. In situ X-ray diffraction patterns for x = 0.10 at different temperatures, registered from 30 to 600 °C.

Table 2. Curie Temperatures,[a] Phase Transitions, and Cell Parameters

			cell parameters				
composition (x)	T_c (°C)	phase transition	T (°C)	a (Å)	b (Å)	c (Å)	$\alpha = \beta = \gamma$ (deg)
0.02	775	*R*3*c* → *Pnma*	820	5.5911	7.8795	5.5643	90
0.07	530	*R*3*c* → *Pbnm*	620	5.4938	5.6138	7.8871	90
0.10	420	*R*3*c* + *Pbnm* → *Pbnm*	600	5.4774	5.6294	7.9052	90

[a]Curie temperatures were obtained by DSC, TMA, and temperature-dependent XRD.

DOI: 10.1021/acs.inorgchem.5b01654
Inorg. Chem. 2015, 54, 9876−9884

air as a function of temperature, from 30 to 600 °C, in intervals of 10 °C upon stepwise heating and in the 2θ range from 20° to 35°. The patterns from 30 °C to ~420 °C are identical, indicating no phase transition in this temperature range, and they exhibit peaks corresponding to the starting mixture of *R*3*c* phase with 6% residual *Pbnm* phase, as presented in Figures 3 and 4. From 420 °C to ~600 °C, the intensities of the weak peaks at 25.4°, 32.7°, and 33.8°, which correspond to the *Pbnm* structure, increase and the single peak at 22.5° splits into two overlapped peaks. Moreover, the intensity of the left-hand peak in the pair at 32° decreases. Therefore, the crystal structure evolves upon heating from *R*3*c* to *Pbnm* phase, which is obtained as a single phase at 600 °C. The crystal structure was indexed at 600 °C by use of the Celref software, and the cell parameters obtained are included in Table 2.

The same procedure was employed to study the ferroelectric−paraelectric phase transitions for x = 0.02 and 0.07 (see Supporting Information, Figures S5 and S6). The transitions take place in the same temperature range as observed by DSC and thermomechanical analysis (TMA). Moreover, for x = 0.07, a phase transition between *R*3*c* and orthorhombic *Pbnm* structure is observed, as detected for x = 0.10. On the other hand, for x = 0.02, the high-temperature phase corresponds to *Pnma*, which may be related to the small amount of yttrium in this phase since the phase transition from *R*3*c* to *Pnma* structure has also been observed for $BiFeO_3$. High-temperature phases were indexed by use of the Celref software, at 820 and 620 °C for x = 0.02 and 0.07, respectively, and the cell parameters are also included in Table 2.

The nature of the optical band gap (E_g) of the samples was studied by diffuse reflectance spectroscopy, since the UV−vis absorption performance of a semiconductor is closely correlated with its energy band. Figure 10 presents, as an

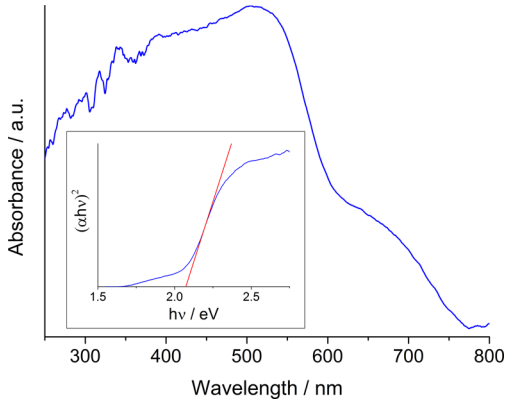

Figure 10. Diffuse reflectance spectrum for composition x = 0.07. (Inset) Band gap calculated by means of Tauc's plot.

example, the registered diffuse reflectance spectrum for composition x = 0.07, converted to the Kubelka−Munk function in order to obtain the absorption coefficient (α).[62,63] The absorption cutoff wavelength is about 600 nm and a slight absorption is also observed from ~650 nm. Similar behavior was observed for compositions x = 0.02 and 0.10 (see Supporting Information, Figures S7 and S8). Tauc's plot is a commonly used method to determine the band gap in semiconductors,[64] which is based on the following expression:

$$(h\nu\alpha)^{1/n} = A(h\nu - E_g) \quad (2)$$

where h is Planck's constant, ν is frequency, A is a proportional constant, and E_g is optical band gap energy in electronvolts. The value of n depends on the type of optical transition when a photon is absorbed. Thus, n = $^1/_2$, $^3/_2$, 2, and 3 for direct allowed, direct forbidden, indirect allowed, and indirect forbidden transitions, respectively.[64] For $BiFeO_3$ and related materials the band gap is direct (n = $^1/_2$),[65−68] and the plot of $(\alpha h\nu)^2$ versus $h\nu$ is drawn. The tangent to the point of inflection on the curve is drawn and the $h\nu$ value at the intercept of the line on the abscissa is the band gap E_g value (inset, Figure 10). The calculated values for E_g are 2.09, 2.07, and 2.04 for x = 0.02, 0.07, and 0.10, respectively. Therefore, the optical band gap decreases with increasing yttrium content, unlike the results reported by Mukherjee et al.[36] Moreover, these values of E_g are lower than those reported by other authors for Y-substituted $BiFeO_3$.[32] These results suggest that the obtained samples are promising visible-light photocatalysts.

Temperature-dependent impedance measurements showed that all samples present high resistivity at room temperature and presented modest levels of semiconductivity from approximately 275 °C. Figure 11 presents impedance data for

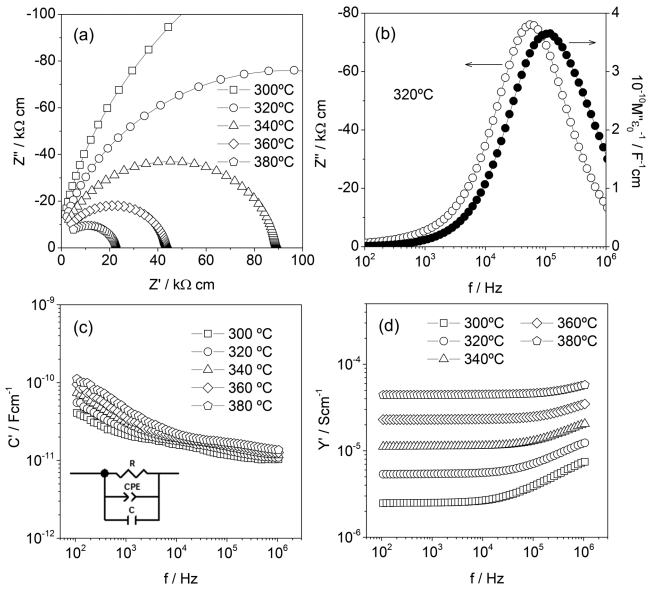

Figure 11. (a) Impedance plots, (b) Z''/M'' spectroscopic plots, and (c) C' and (d) Y' vs frequency for $Bi_{0.98}Y_{0.02}FeO_3$ obtained after 6 h of mechanical activation and subsequent sintering at 850 °C.

x = 0.02 in the temperature range from 300 to 380 °C. Impedance complex plane plots (Figure 11a) show single but distorted arcs whose low-frequency intercepts give total resistance of the sample at each temperature. M'' and Z'' spectroscopic plots measured at 320 °C (Figure 11b) show single broad peaks with very small differences in the frequency of their maxima, which may indicate that the samples are electrically homogeneous. Capacitance data (Figure 11c) show high-frequency plateaus at approximately 10−14 pF·cm^{-1}, which correspond to the bulk response of the sample. A small increase in C' is observed at low frequencies, which could indicate a power law response. Conductivity plots (Figure 11d) show low-frequency plateaus followed by dispersion at high frequencies, indicating again a possible power law response.[69,70] It can be estimated that the equivalent circuit for these data is composed by a parallel R−C−CPE element shown in the inset

DOI: 10.1021/acs.inorgchem.5b01654
Inorg. Chem. 2015, 54, 9876−9884

of Figure 11c, where R is a resistor, C is a capacitor, and CPE is a constant phase element responsible for the dispersion observed in C' at low frequencies and Y' at high frequencies. A similar behavior has been observed for $BiFeO_3$ and La-substituted $BiFeO_3$ ($0 \leq x \leq 0.15$) samples prepared by direct mechanosynthesis.[49,57,71]

Resistance values as a function of temperature, obtained from intercepts on the real Z' axis of the impedance complex plane plots, are shown in Arrhenius format (log σ against inverse temperature, where σ is conductivity) in Figure 12 for the three

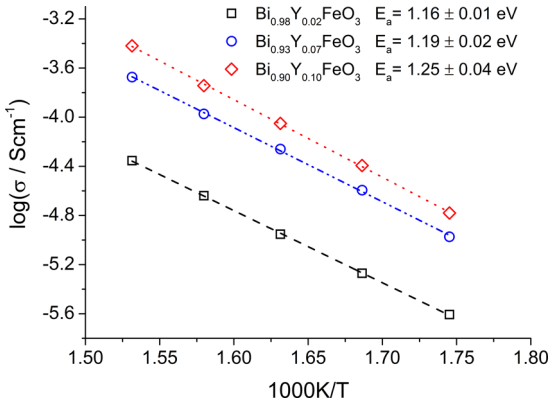

Figure 12. Bulk conductivity data for $Bi_{1-x}Y_xFeO_3$ ceramics.

samples prepared, measured from 300 to 380 °C. The resistivity at room temperature, extrapolated from the Arrhenius plots, is in the range $\sim 10^{15}-(9 \times 10^{13})$ Ω·cm. The conductivity is small and increases with increasing yttrium content with a slight increase in the activation energies, calculated from the slopes of the plots. This result suggests an increase in the number of charge carriers with x, as has been reported for samples of the system $Bi_{1-x}La_xFeO_3$ ($0 \leq x \leq 0.15$).[49,57] The low conductivity of the samples indicates that mixed valence of Fe and oxygen nonstoichiometry have been avoided by the methodology employed to prepare the samples. The conduction mechanism was investigated by registering impedance data in air, oxygen, and nitrogen at 350 °C, as presented in Figure 13 for composition $x = 0.10$. As may be observed in the figure, the resistivity of the sample decreases as the partial pressure of oxygen increases, which suggests that the conduction is p-type. Samples $x = 0.02$ and 0.07 presented identical behavior (see

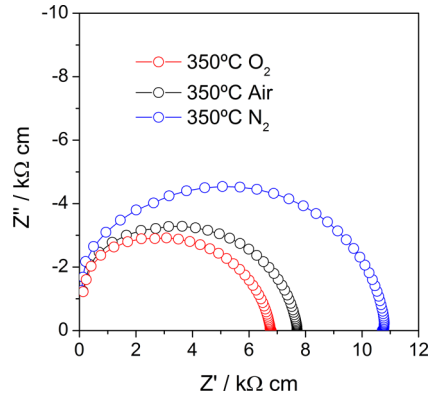

Figure 13. Impedance complex plane plots at 350 °C in oxygen, air, and nitrogen for $Bi_{0.90}Y_{0.10}FeO_3$.

Supporting Information, Figures S9 and S10). Therefore, the samples can pick up oxygen by the mechanism:

$$O_2 \rightarrow 2O^{2-} + 4h^{\bullet} \quad (3)$$

Although the results shown in Figure 13 allow identifying holes as the main charge carrier in Y-substituted $BiFeO_3$, the origin of the holes is not known, and further investigation to determine the charge compensation mechanism is needed.

4. CONCLUSIONS

Dense $Bi_{1-x}Y_xFeO_3$ ($x = 0.02$, 0.07, and 0.10) pellets have been prepared by mechanical activation and sintering at 850 °C. Single-phase materials have been obtained for $x = 0.02$ and 0.07, with rhombohedral $R3c$ structure, as assayed by Raman spectroscopy and X-ray diffraction analysis. On the other hand, a mixture of 94% rhombohedral $R3c$ and 6% orthorhombic $Pbnm$ structures has been detected by Rietveld analysis for $x = 0.10$. EDX semiquantitave analysis revealed that the materials maintained the nominal stoichiometry after mechanical treatment and sintering. The multiferroic character of the samples was studied by DSC, dilatometry, and high-temperature X-ray diffraction. Thus, a slight decrease in the antiferromagnetic–paramagnetic transition at T_N with increasing yttrium content is observed, and the ferroelectric–paraelectric transition at T_C also decreases, from 775 °C for $x = 0.02$ to 530 °C for $x = 0.07$. For $x = 0.10$, the Curie temperature was observed by dilatometry and high-temperature X-ray diffraction that suggest that the phase transition takes place over a wide range of temperatures. Moreover, the nature of the ferroelectric–paraelectric phase transitions was studied by temperature-dependent XRD, which showed rhombohedral to orthorhombic phase transitions in all cases. High-temperature phases were indexed as $Pnma$ for $x = 0.02$ and $Pbnm$ for $x = 0.07$ and 0.10. Diffuse reflectance spectroscopic measurements allowed determining that the samples present low optical band gap, which could imply that they are promising visible-light photocatalysts. Moreover, the samples are electrically homogeneous, as deduced from impedance spectroscopy measurements, with low conductivity that increases with increasing yttrium content and a p-type conduction mechanism.

■ ASSOCIATED CONTENT

Supporting Information

The Supporting Information is available free of charge on the ACS Publications website at DOI: 10.1021/acs.inorgchem.5b01654.

Ten figures showing dilatometric curves of pellets, Rietveld refinements, high-temperature powder XRD patterns, diffuse reflectance spectra, and impedance complex plane plots at 350 °C in oxygen, air, and nitrogen (PDF)

■ AUTHOR INFORMATION

Corresponding Authors

*E-mail antonio.perejon@icmse.csic.es; tel (+34) 95 448 95 00; fax (+34) 95 446 01 65 (A.P.).

*E-mail maqueda@cica.es; tel (+34) 95 448 95 48; fax (+34) 95 446 01 65 (L.A.P.-M.).

Notes

The authors declare no competing financial interest.

DOI: 10.1021/acs.inorgchem.5b01654
Inorg. Chem. 2015, 54, 9876–9884

■ ACKNOWLEDGMENTS

Financial support from Projects CTQ2014-52763-C2-1-R (MINECO-FEDER), TEP-7858 (Junta Andalucía-FEDER), and TEP-1900 (Junta Andalucía-FEDER) is acknowledged. The authors also thank VPPI-US for the AP current contract. Additionally, P.E.S.-J. is supported by a Marie Curie−Junta de Andalucía Talentia grant.

■ REFERENCES

(1) Eerenstein, W.; Mathur, N. D.; Scott, J. F. *Nature* **2006**, *442*, 759−765.
(2) Fiebig, M. *J. Phys. D: Appl. Phys.* **2005**, *38*, R123−R152.
(3) Schmid, H. *Ferroelectrics* **1994**, *162*, 317−338.
(4) Bibes, M.; Barthelemy, A. *Nat. Mater.* **2008**, *7*, 425−426.
(5) Cheong, S.-W.; Mostovoy, M. *Nat. Mater.* **2007**, *6*, 13−20.
(6) Spaldin, N. A.; Cheong, S.-W.; Ramesh, R. *Phys. Today* **2010**, *63*, 38−43.
(7) Spaldin, N. A.; Fiebig, M. *Science* **2005**, *309*, 391−392.
(8) Catalan, G.; Scott, J. F. *Adv. Mater.* **2009**, *21*, 2463−2485.
(9) Ederer, C.; Spaldin, N. A. *Phys. Rev. B: Condens. Matter Mater. Phys.* **2005**, *71*, No. 060401.
(10) Das, S. R.; Choudhary, R. N. P.; Bhattacharya, P.; Katiyar, R. S.; Dutta, P.; Manivannan, A.; Seehra, M. S. *J. Appl. Phys.* **2007**, *101*, No. 034104.
(11) Wang, Y. P.; Zhou, L.; Zhang, M. F.; Chen, X. Y.; Liu, J.-M.; Liu, Z. G. *Appl. Phys. Lett.* **2004**, *84*, 1731−1733.
(12) Safi, R.; Shokrollahi, H. *Prog. Solid State Chem.* **2012**, *40*, 6−15.
(13) Chen, J.; Xing, X.; Watson, A.; Wang, W.; Yu, R.; Deng, J.; Yan, L.; Sun, C.; Chen, X. *Chem. Mater.* **2007**, *19*, 3598−3600.
(14) Kim, J. K.; Kim, S. S.; Kim, W. J. *Mater. Lett.* **2005**, *59*, 4006−4009.
(15) Valant, M.; Axelsson, A.-K.; Alford, N. *Chem. Mater.* **2007**, *19*, 5431−5436.
(16) Buscaglia, M. T.; Mitoseriu, L.; Buscaglia, V.; Pallecchi, I.; Viviani, M.; Nanni, P.; Siri, A. S. *J. Eur. Ceram. Soc.* **2006**, *26*, 3027−3030.
(17) Kumar, M. M.; Srinivas, A.; Suryanarayana, S. V. *J. Appl. Phys.* **2000**, *87*, 855−862.
(18) Zhu, W. M.; Ye, Z. G. *Appl. Phys. Lett.* **2006**, *89*, 232904.
(19) Correas, C.; Hungria, T.; Castro, A. *J. Mater. Chem.* **2011**, *21*, 3125−3132.
(20) Wang, Q. Q.; Wang, Z.; Liu, X. Q.; Chen, X. M. *J. Am. Ceram. Soc.* **2012**, *95*, 670−675.
(21) Kanai, T.; Ohkoshi, S.; Nakajima, A.; Watanabe, T.; Hashimoto, K. *Adv. Mater.* **2001**, *13*, 487−490.
(22) Belik, A. A. *Inorg. Chem.* **2013**, *52*, 2015−2021.
(23) Sosnowska, I.; Azuma, M.; Przeniosło, R.; Wardecki, D.; Chen, W.-t.; Oka, K.; Shimakawa, Y. *Inorg. Chem.* **2013**, *52*, 13269−13277.
(24) Kubota, M.; Oka, K.; Yabuta, H.; Miura, K.; Azuma, M. *Inorg. Chem.* **2013**, *52*, 10698−10704.
(25) Dutta, D. P.; Jayakumar, O. D.; Tyagi, A. K.; Girija, K. G.; Pillai, C. G. S.; Sharma, G. *Nanoscale* **2010**, *2*, 1149−1154.
(26) Catalan, G.; Sardar, K.; Church, N. S.; Scott, J. F.; Harrison, R. J.; Redfern, S. A. T. *Phys. Rev. B: Condens. Matter Mater. Phys.* **2009**, *79*, No. 212415.
(27) Hu, W.; Chen, Y.; Yuan, H.; Li, G.; Qiao, Y.; Qin, Y.; Feng, S. *J. Phys. Chem. C* **2011**, *115*, 8869−8875.
(28) Rusakov, D. A.; Abakumov, A. M.; Yamaura, K.; Belik, A. A.; Van Tendeloo, G.; Takayama-Muromachi, E. *Chem. Mater.* **2011**, *23*, 285−292.
(29) Yang, C. H.; Kan, D.; Takeuchi, I.; Nagarajan, V.; Seidel, J. *Phys. Chem. Chem. Phys.* **2012**, *14*, 15953−15962.
(30) Clemens, O.; Kruk, R.; Patterson, E. A.; Loho, C.; Reitz, C.; Wright, A. J.; Knight, K. S.; Hahn, H.; Slater, P. R. *Inorg. Chem.* **2014**, *53*, 12572−12583.
(31) Cheng, Z. X.; Li, A. H.; Wang, X. L.; Dou, S. X.; Ozawa, K.; Kimura, H.; Zhang, S. J.; Shrout, T. R. *J. Appl. Phys.* **2008**, *103*, No. 07E507.
(32) Bellakki, M. B.; Manivannan, V. *J. Sol-Gel Sci. Technol.* **2010**, *53*, 184−192.
(33) Wu, Y. J.; Chen, X. K.; Zhang, J.; Chen, X. J. *J. Magn. Magn. Mater.* **2012**, *324*, 1348−1352.
(34) Luo, M.; Zhou, P. H.; Liu, Y. F.; Wang, X.; Xie, J. L. *Phys. B* **2014**, *450*, 1−6.
(35) Mishra, R. K.; Pradhan, D. K.; Choudhary, R. N. P.; Banerjee, A. *J. Phys.: Condens. Matter* **2008**, *20*, 045218.
(36) Mukherjee, A.; Basu, S.; Chakraborty, G.; Pal, M. *J. Appl. Phys.* **2012**, *112*, No. 014321.
(37) Minh, N. V.; Thang, D. V. *J. Alloys Compd.* **2010**, *505*, 619−622.
(38) Singh, V.; Sharma, S.; Dwivedi, R. K.; Kumar, M.; Kotnala, R. K.; Mehra, N. C.; Tandon, R. P. *J. Supercond. Novel Magn.* **2013**, *26*, 657−661.
(39) Feng, B. L.; Xue, H.; Xiong, Z. X. *Chin. Sci. Bull.* **2010**, *55*, 452−456.
(40) Medina, L. M. S.; Jorge, G. A.; Negri, R. M. *J. Alloys Compd.* **2014**, *592*, 306−312.
(41) Luo, L. R.; Wei, W.; Yuan, X. Y.; Shen, K.; Xu, M. X.; Xu, Q. Y. *J. Alloys Compd.* **2012**, *540*, 36−38.
(42) Kong, L. B.; Zhang, T. S.; Ma, J.; Boey, F. *Prog. Mater. Sci.* **2008**, *53*, 207−322.
(43) Da Silva, K. L.; Menzel, D.; Feldhoff, A.; Kuebel, C.; Bruns, M.; Paesano, A., Jr.; Duevel, A.; Wilkening, M.; Ghafari, M.; Hahn, H.; Litterst, F. J.; Heitjans, P.; Becker, K. D.; Sepelak, V. *J. Phys. Chem. C* **2011**, *115*, 7209−7217.
(44) Sepelak, V.; Duevel, A.; Wilkening, M.; Becker, K.-D.; Heitjans, P. *Chem. Soc. Rev.* **2013**, *42*, 7507−7520.
(45) Balaz, P.; Achimovicova, M.; Balaz, M.; Billik, P.; Cherkezova-Zheleva, Z.; Criado, J. M.; Delogu, F.; Dutkova, E.; Gaffet, E.; Gotor, F. J.; Kumar, R.; Mitov, I.; Rojac, T.; Senna, M.; Streletskii, A.; Wieczorek-Ciurowa, K. *Chem. Soc. Rev.* **2013**, *42*, 7571−7637.
(46) Perejon, A.; Murafa, N.; Sanchez-Jimenez, P. E.; Criado, J. M.; Subrt, J.; Dianez, M. J.; Perez-Maqueda, L. A. *J. Mater. Chem. C* **2013**, *1*, 3551−3562.
(47) Rietveld, H. M. *J. Appl. Crystallogr.* **1969**, *2*, 65−71.
(48) Rodriguez-Carvajal, J. *Short Reference Guide of the FullProf Program, Version 3.5*; Laboratory Leon Brilloium (CEA-CNRS), 1997.
(49) Perejon, A.; Sanchez-Jimenez, P. E.; Perez-Maqueda, L. A.; Criado, J. M.; de Paz, J. R.; Saez-Puche, R.; Maso, N.; West, A. R. *J. Mater. Chem. C* **2014**, *2*, 8398−8411.
(50) Bellakki, M. B.; Manivannan, V.; Madhu, C.; Sundaresan, A. *Mater. Chem. Phys.* **2009**, *116*, 599−602.
(51) Suresh, P.; Srinath, S. *J. Alloys Compd.* **2013**, *554*, 271−276.
(52) Yang, Y.; Liu, Y. L.; Zhu, K.; Zhang, L. Y.; Ma, S. Y.; Liu, J. E.; Jiang, Y. J. *Chin. Phys. B* **2010**, *19*, No. 037802.
(53) Khodabakhsh, M.; Sen, C.; Khassaf, H.; Gulgun, M. A.; Misirlioglu, I. B. *J. Alloys Compd.* **2014**, *604*, 117−129.
(54) Bielecki, J.; Svedlindh, P.; Tibebu, D. T.; Cai, S. Z.; Eriksson, S. G.; Borjesson, L.; Knee, C. S. *Phys. Rev. B: Condens. Matter Mater. Phys.* **2012**, *86*, No. 184422.
(55) Karpinsky, D. V.; Troyanchuk, I. O.; Mantytskaya, O. S.; Khomchenko, V. A.; Kholkin, A. L. *Solid State Commun.* **2011**, *151*, 1686−1689.
(56) Arnold, D. C. *IEEE Trans. Ultrason. Ferroelectr. Freq. Control* **2015**, *62*, 62−82.
(57) Perejon, A.; Sanchez-Jimenez, P. E.; Poyato, R.; Maso, N.; West, A. R.; Criado, J. M.; Perez-Maqueda, L. A. *J. Eur. Ceram. Soc.* **2015**, *35*, 2283−2293.
(58) Goldschmidt, V. M. *Naturwissenschaften* **1926**, *14*, 477−485.
(59) Shannon, R. D. *Acta Crystallogr., Sect. A: Cryst. Phys., Diffr., Theor. Gen. Crystallogr.* **1976**, *32*, 751−767.
(60) Gautam, A.; Singh, K.; Sen, K.; Kotnala, R. K.; Singh, M. *Mater. Lett.* **2011**, *65*, 591−594.
(61) Srivastav, S. K.; Gajbhiye, N. S.; Banerjee, A. *J. Appl. Phys.* **2013**, *113*, No. 203917.
(62) Kubelka, P.; Munk, F. *Z. Tech. Phys.* **1931**, *12*, 593−601.
(63) Gao, F.; Chen, X. Y.; Yin, K. B.; Dong, S.; Ren, Z. F.; Yuan, F.; Yu, T.; Zou, Z.; Liu, J. M. *Adv. Mater.* **2007**, *19*, 2889−2892.

DOI: 10.1021/acs.inorgchem.5b01654
Inorg. Chem. 2015, 54, 9876−9884

(64) Tauc, J.; Grigorovici, R.; Vancu, A. *Phys. Status Solidi B* **1966**, *15*, 627−637.
(65) Ihlefeld, J. F.; Podraza, N. J.; Liu, Z. K.; Rai, R. C.; Xu, X.; Heeg, T.; Chen, Y. B.; Li, J.; Collins, R. W.; Musfeldt, J. L.; Pan, X. Q.; Schubert, J.; Ramesh, R.; Schlom, D. G. *Appl. Phys. Lett.* **2008**, *92*, No. 142908.
(66) Xu, Y.; Shen, M. *Mater. Lett.* **2008**, *62*, 3600−3602.
(67) Takahashi, K.; Kida, N.; Tonouchi, M. *Phys. Rev. Lett.* **2006**, *96*, No. 117402.
(68) Ortiz-Quinonez, J. L.; Diaz, D.; Zumeta-Dube, I.; Arriola-Santamaria, H.; Betancourt, I.; Santiago-Jacinto, P.; Nava-Etzana, N. *Inorg. Chem.* **2013**, *52*, 10306−10317.
(69) Jonsher, A. K. *Dielectric Relaxation in Solids*; Chelsea Dielectric Press: London, 1983.
(70) Jonsher, A. K. *Universal Relaxation Law*; Chelsea Dielectric Press: London, 1996.
(71) Perejon, A.; Maso, N.; West, A. R.; Sanchez-Jimenez, P. E.; Poyato, R.; Criado, J. M.; Perez-Maqueda, L. A. *J. Am. Ceram. Soc.* **2013**, *96*, 1220−1227.

DOI: 10.1021/acs.inorgchem.5b01654
Inorg. Chem. 2015, 54, 9876−9884